Chinese Chemical Letters 35 (2024) 108921

Contents lists available at ScienceDirect

Chinese Chemical Letters

journal homepage: www.elsevier.com/locate/cclet

Carbon dots confined nanosheets assembled $NiCo_2S_4$@CDs cross-stacked architecture for enhanced sodium ion storage

Binyang Qin, Mengqi Wang, Shimei Wu, Yining Li, Chilin Liu, Yufei Zhang*, Haosen Fan*

School of Chemistry and Chemical Engineering, Guangzhou University, Guangzhou 510006, China

ARTICLE INFO

Article history:
Received 9 June 2023
Revised 31 July 2023
Accepted 9 August 2023
Available online 13 August 2023

Keywords:
Carbon dots
Sodium ion batteries
$NiCo_2S_4$@CDs
Cross-stacked architecture
Ex-situ XRD and XPS

ABSTRACT

Na^+ batteries (SIBs) have been emerging as the most promising candidate for the next generation of secondary batteries. However, the development of high-performance and cost-effective anode materials is urgently needed for the large-scale applications of SIBs. In this study, carbon dots confined bimetallic sulfide ($NiCo_2S_4$) architecture ($NiCo_2S_4$@CDs) was proposed and synthesized from assembling nanosheets into cross-stacked superstructure and the subsequent confinement of carbon dots. This novel decussated structure assembly from nanosheets is greatly beneficial to the structure stability of electrode material during the successive charge/discharge processes. Besides, the CDs based carbon conductive network can enhance the electrical conductivity for facilitating the easy transport of electron/Na^+. Benefitting from these advantages, $NiCo_2S_4$@CDs exhibits high-rate performance and an ultralong cycling life in SIBs. Specifically, the specific capacity of $NiCo_2S_4$@CDs can reach the discharge specific capacity as high as 568.9 mAh/g at 0.5 A/g, which can also maintain 302.7 mAh/g after 750 cycles at 5.0 A/g. Additionally, *ex-situ* characterization techniques such as *ex-situ* XRD and *ex-situ* XPS were employed to further explore the sodium storage mechanism of the $NiCo_2S_4$@CDs anode.

Advanced energy storage technology is essential for exploiting future sustainable and renewable energy supply. Lithium–ion batteries (LIBs) are commonly utilized as a power source for a series of applications, containing portable electronics and transportation, owing to their high energy density and extended lifespan [1–4]. However, the scarcity and costly nature of lithium resources have become a challenge due to the continuously growing need for energy storage solutions in the market, making it increasingly difficult for lithium for the future energy demands. Sodium, as an element with the same group as lithium, exhibits comparable chemical characteristics to lithium. Besides, sodium–ion batteries (SIBs) display similar electrochemical behavior to that of LIBs, which endowed SIBs as promising alternative to LIBs. However, the electrochemical reaction kinetics and storage capacity of SIBs are inevitably suppressed owing to the larger ionic radii of Na^+ (1.02 Å) in comparison with Li^+ (0.76 Å), as well as the high relative atomic masses of Na (23, 6.9 for Li) [5–7]. Therefore, developing anode materials that have high reversible capacity and stable cycling performance for Na^+ storage is a critical challenge for SIBs [8–10].

Transition metal sulfides (TMSs) have become one of the best electrode materials for SIBs due to their excellent theoretical capacity and abundant active sites [11,12]. Moreover, compared to single-metal sulfides, mixed metal sulfides (MMSs) have received growing interest in the energy storage domain thanks to their ability to generate synergistic effects, possess lower band gaps and higher conductivity [13]. $Ni_xCo_{3-x}S_4$ compound is a promising electrode material for SIBs, as it exhibits richer redox reactions and higher specific capacitance compared to its respective single-metal sulfides (NiS_x/CoS_x) [14,15]. However, the cycle life and rate performance of $Ni_xCo_{3-x}S_4$ are hindered by volumetric expansion that occurs during the redox process. According to literature reports, structural engineering that enhances material stability is an effective means of improving volume expansion [16]. For example, Li *et al.* synthesized nickel boride (Ni–B) nanosheets within hollow Ni–Co sulfide nanospheres and found that the Ni–B component could reinforce the structural stability of the electrode material. The reversible capacity after 200 cycles at 1.0 A/g was 251.9 mAh/g, which represented a significant improvement over bare $NiCo_2S_4$ [17]. Liu *et al.* synthesized $NiCo_2S_4$@MoS_2 core-shell nanostructures *via* a hydrothermal method, which enhance the contact between the electrolyte and the core/shell nanostructure and promote the rate of Na^+ diffusion. At 6.4 A/g, a capacity of 155 mAh/g was delivered, and the Coulombic efficiency remained above 99% after 400 cycles [18]. In addition, introducing a highly conductive and buffering matrix is considered a highly effective approach,

* Corresponding authors.
E-mail addresses: yfzhang@gdut.edu.cn (Y. Zhang), hsfan@gzhu.edu.cn (H. Fan).

https://doi.org/10.1016/j.cclet.2023.108921
1001-8417/

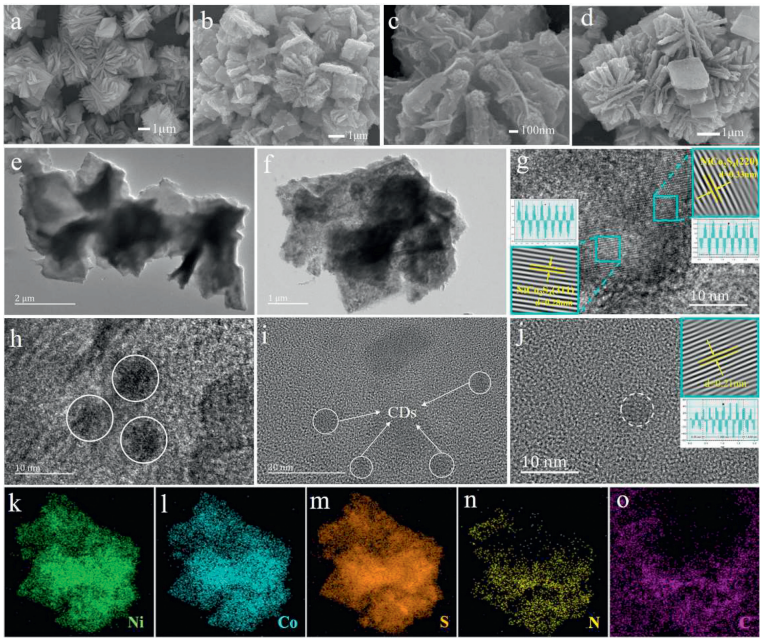

Fig. 1. SEM of (a) NiCoCP, (b) $NiCo_2S_4$, (c, d) $NiCo_2S_4$@CDs. (e, f) TEM images of $NiCo_2S_4$@CDs. (g) HRTEM image of $NiCo_2S_4$@CDs, inset in (g) shows the inverse FFT patterns. (h–j) HRTEM image of CDs in $NiCo_2S_4$@CDs, inset in (j) shows the inverse FFT patterns. (k–o) Mapping images of $NiCo_2S_4$@CDs.

such as the introduction of carbon materials, which can effectively suppress the volume expansion and prevent their self-aggregation, thereby improving the cycling life of the electrode material [19–22]. Sun *et al*. synthesized $NiCo_2S_4$@rGO nanocomposites with reduced graphene oxide (rGO) as a protective matrix. The rGO coating effectively immobilized the transformation products of NiS_2 and CoS_2 generated during the phase transition of $NiCo_2S_4$, thereby enhancing the structural stability and mitigating volumetric expansion. As a result, the $NiCo_2S_4$@rGO composite maintained a capacity retention rate of over 95% after 100 cycles, while exhibiting a high reversible capacity of 621 mAh/g at 0.1 A/g [23]. Fan *et al*. immobilized $NiCo_2S_4$ nanosheets onto the surface of carbon nanotubes (CNTs), which reduced the impact of volume expansion on $NiCo_2S_4$ and increased the conductivity of the composite electrode material. The $NiCo_2S_4$@CNTs electrode showed a capacity of 169.29 mAh/g (10 A/g) in SIBs [24]. Despite their excellent electrochemical performance, both reduced graphene oxide and carbon nanotubes face high costs that hinder their further development and application. Therefore, it is imperative to investigate novel and cost-effective carbon material composite electrodes. Carbon dots (CDs), as a new type of zero-dimensional (0D) carbon material with ultra-small particle size (less than 10 nm), can greatly alleviate the aggregation of composite materials, improve their conductivity, and provide stable support for the structure of the composite material [25–28]. Compared to traditional carbon materials, the introduction of CDs shows great potential for further exploration.

Recently, coordination polymers (CPs), also called metal–organic framework materials (MOFs), constructing by the combination of metal ions and organic ligands, have been acknowledged as a highly effective category of electrochemical energy storage materials owing to their exceptional strengths in tunable pore structures and high specific surface areas [29–31]. In this study, nickel-cobalt bimetal coordination polymer (NiCoCP) was firstly synthesized by a co-precipitation method and used as a sacrificial template. Then, $NiCo_2S_4$@CDs cross-stacked architecture was obtained through high-temperature sulfidation of NiCoCP and the subsequent carbon coating process from the carbonization of glucose. These carbon dots (CDs) loaded in $NiCo_2S_4$ can effectively increase the conductivity of the electrode material. When employed as anodes in SIBs, $NiCo_2S_4$@CDs delivered a rate capacity of 568.9 mAh/g at 0.5 A/g and could maintain a discharge specific capacity of 302.7 mAh/g after 750 cycles at 5.0 A/g.

The process for synthesizing the $NiCo_2S_4$@CDs with hierarchical layered structure decorated with carbon dots is illustrated in Fig. S1 (Supporting information). Initially, NiCoCP precursors were prepared using the coprecipitation method. Nanosheets of nickel-cobalt bimetallic polymer assembled through static adsorption between $Ni(CN)_4^{2-}$ and Co^{2+} ions. Sodium citrate was used to induce self-assembly, resulting in the formation of cross-stacked cubic nanoflowers. Afterwards, the NiCoCP precursor underwent additional high temperature sulfidation treatment to yield nickel-cobalt bimetallic sulfide $NiCo_2S_4$. This transition metal sulfide was derived from metal-organic frameworks (MOFs), and was characterized by abundant internal pores, providing the possibility of loading glucose. $NiCo_2S_4$ loaded with glucose was then heated at 200 °C for 3 h, causing the carbonization of glucose into carbon dots. This ultimately resulted in the formation of $NiCo_2S_4$@CDs with a hierarchical layered structure decorated with carbon dots.

The morphology and structure of the samples were characterized using SEM, TEM, and EDS techniques. The SEM images of the precursor NiCoCP are displayed in Fig. 1a, from which the morphology of this material can be visually observed to consist of uniformly sized and evenly dispersed 3D cubic nanoflowers, each of which is composed of multiple smooth nanosheets that cross-stack with each other. Fig. 1b illustrates SEM images of $NiCo_2S_4$ after undergoing high-temperature sulfidation treatment, revealing the retention of the basic morphology of the NiCoCP precursor while exhibiting a rougher surface. Upon magnification, numerous small nanoparticles are observed on the surface. Figs. 1c and d presents SEM images of the final sample, $NiCo_2S_4$@CDs. While the surface morphology is similar to that of $NiCo_2S_4$, significant internal changes have taken place, which will be further elucidated in subsequent investigations. The TEM images of $NiCo_2S_4$@CDs are presented in Figs. 1e and j, which confirms that the nanoflowers in $NiCo_2S_4$@CDs are composed of multiple nanosheets cross-stacked with each other. The HRTEM image of $NiCo_2S_4$@CDs displayed in Fig. 1g shows two sets of lattice fringes corresponding to the 311 plane (d = 0.28 nm) and 220 plane (d = 0.33 nm) of the $NiCo_2S_4$

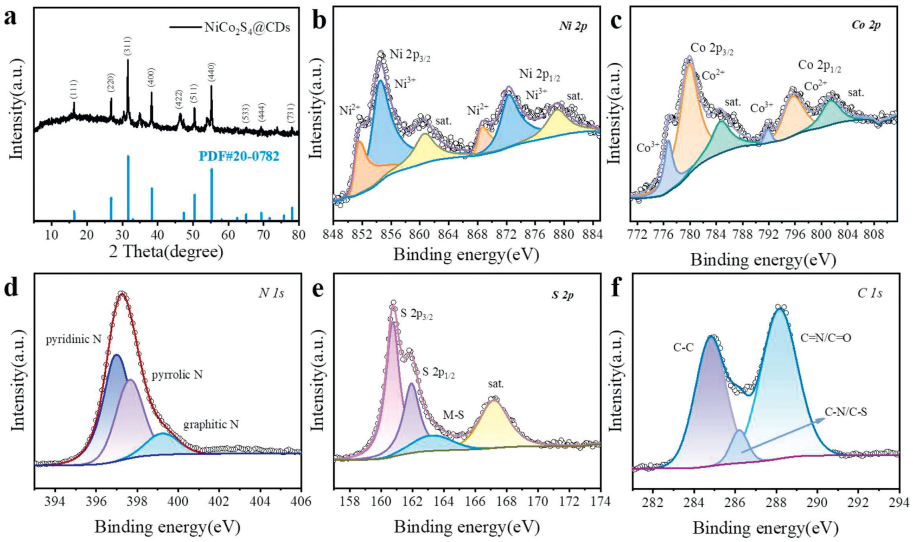

Fig. 2. (a) XRD pattern of $NiCo_2S_4$@CDs. High-resolution XPS spectrum of (b) Ni 2p, (c) Co 2p, (d) N 1s, (e) S 1s, (f) C 1s.

phase. The HRTEM images of the CDs in $NiCo_2S_4$@CDs depicted in Figs. 1h–j show that the CDs have a size range below 10 nm, and the insert in Fig. 1j reveals a lattice spacing of 0.21 nm that matches well with the (100) plane of graphite carbon, thereby confirming the formation of CDs. Figs. 1k-o display the EDS analysis results, which confirms the presence of Ni, Co, S, N, and C elements in the synthesized $NiCo_2S_4$@CDs, thereby validating its successful synthesis.

The XRD spectra were used to study the information of the purity and crystal structure of the prepared samples. Fig. 2a displays the XRD diffraction pattern of the target product, showing characteristic peaks at 16.3°, 26.8°, 31.5°, 38.3°, 46.4°, 50.4°, 55.2°, 65.1°, 69.2°, and 78.0° that correspond to the (111), (220), (311), (400), (422), (511), (440), (533), (444), and (731) lattice planes of cubic phase $NiCo_2S_4$@CDs according to JCPDS card No. 20-0782. The diffraction peaks of the sample are clear and sharp, with no excess peaks observed, indicating its high crystallinity. XPS analysis was performed to examine the surface elemental composition and electron structure of the $NiCo_2S_4$@CDs nanocomposite material. Fig. S2 (Supporting information) presents the complete measurement spectrum of the composite material in the 0–1400 eV range, revealing six types of characteristic peaks that indicate the presence of Ni, Co, S, C, N, and O elements. The presence of the O element can be explained by the surface oxidation of the material. The peaks observed at 860.7 and 879.1 eV in Fig. 2b correspond to satellite peaks of Ni 2p, while the peaks at 851.6/868.7 eV and 854.5/872.4 eV can be ascribed to Ni^{2+} and Ni^{3+}, respectively [32–34]. The Co 2p signal spectrum in Fig. 2c was fitted as Co $2p_{3/2}$ (776.8/780.0 eV) and Co $2p_{1/2}$ (791.9 eV/795.8 eV) two spin–orbit double peaks, indicating that cobalt exists in two states of Co^{3+} and Co^{2+} in the sample, accompanied by two satellite peaks located at 784.8 and 801.6 eV, possibly due to oscillation of high spin Co^{2+} [35–37]. Fig. 2d shows the N 1s fine spectrum. The three characteristic peaks detected at 397.0, 397.7, and 399.2 eV can be assigned to pyridinic nitrogen, pyrrolic nitrogen, and graphitic nitrogen, respectively [38,39]. N doping can introduce more defects, improving electronic conductivity and providing more active sites for Na^+ storage. As shown in Fig. 2e, the S 2p fine spectrum exhibits two prominent peaks located at 160.8 eV and 162.0 eV, which correspond to S^{2-} of S $2p_{3/2}$ and S $2p_{1/2}$, respectively. The peak located at 163.3 eV is attributed to the bonding between S and metals [40,41]. The high-resolution C 1s spectrum shown in Fig. 2f reveals a spectral peak at 284.8 eV corresponding to C–C bonding, another at 286.2 eV attributed to C–N/C–S bonding, and a peak at 288.2 eV corresponding to C=N/C=O bonding [19,42]. All the results indicate the successful preparation of $NiCo_2S_4$@CDs composite material.

Fig. 3 displays the electrochemical properties of the $NiCo_2S_4$@CDs electrode and the $NiCo_2S_4$ contrast sample. To assess their rate performance, the materials were subjected to cycling at different current densities, as illustrated in Fig. 3a. The $NiCo_2S_4$@CDs anode exhibits capacities of 665, 633, 569, 526, 484 and 419 mAh/g at 0.1–5 A/g, respectively. Upon decreasing to 0.2 A/g, the $NiCo_2S_4$@CDs electrode recovers a capacity of 546 mAh/g. In contrast, the $NiCo_2S_4$ electrode demonstrates lower capacity than $NiCo_2S_4$@CDs at the same current density, indicating that $NiCo_2S_4$@CDs exhibits superior rate performance. Fig. 3b shows the discharge/charge curves of $NiCo_2S_4$@CDs and $NiCo_2S_4$ electrodes during the first cycle at 0.1 A/g in SIBs. It is evident that the initial discharge capacity of $NiCo_2S_4$@CDs (854.31 mAh/g) is higher than that of $NiCo_2S_4$ (595.7 mAh/g) during the first cycle. However, the initial Coulombic efficiency of $NiCo_2S_4$@CDs (81.6%) is slightly lower than that of $NiCo_2S_4$ (85.9%) during the first cycle. Fig. 3c illustrates the initial five cycles of charge–discharge curves of $NiCo_2S_4$@CDs at 0.1 A/g. In the first cycle of charging and discharging, the Coulombic efficiency reaches 81%, and in the subsequent cycling process, the charge–discharge curves overlapped well, indicating that $NiCo_2S_4$@CDs demonstrates high reversibility during charging and discharging processes. Fig. 3d depicts the charge–discharge curves of $NiCo_2S_4$@CDs at various current densities, and the curves exhibit two pairs of reaction platforms, corresponding to the outcomes of subsequent cyclic voltammetry (CV) tests. In addition, we compare the rate performance of $NiCo_2S_4$@CDs electrode material with different $NiCo_2S_4$ base electrode materials reported in the literature [13,17,18,23,24,43], as depicted in Fig. 3e. The figure provides a clear depiction of the superior rate performance of the $NiCo_2S_4$@CDs electrode material compared to other $NiCo_2S_4$-based electrode materials, thereby endowing it with highly promising prospects for application in SIBs. Fig. 3f presents the cycle performance of $NiCo_2S_4$@CDs and $NiCo_2S_4$ at 0.5 A/g. Due to inevitable decomposition of electrolyte solution and formation of solid electrolyte interphase (SEI) membrane, the capacity decayed faster in the first few cycles. However, by the 10th cycle, the discharge capacity of $NiCo_2S_4$@CDs stabilizes at 631 mAh/g, while that of $NiCo_2S_4$ only reaches 492 mAh/g. Additionally, the $NiCo_2S_4$@CDs electrode demonstrates outstanding

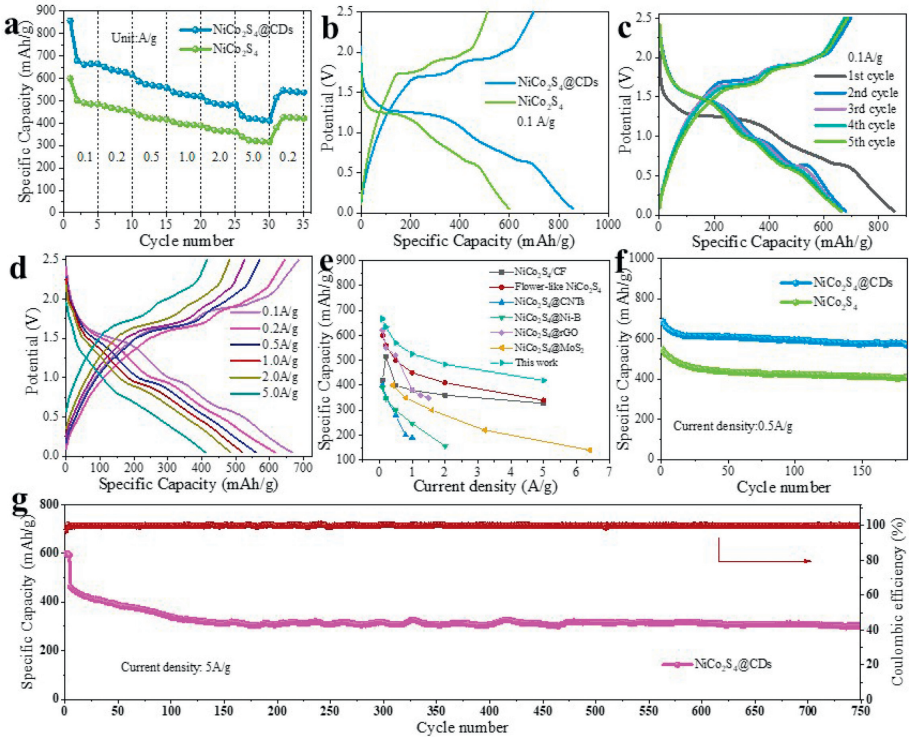

Fig. 3. (a) Rate capability of $NiCo_2S_4$@CDs in SIBs. (b) The discharge/charge curves of $NiCo_2S_4$@CDs and $NiCo_2S_4$ during the first cycle at 0.1 A/g in SIBs. (c) The discharge/charge profiles of $NiCo_2S_4$@CDs at 0.1 A/g in SIBs. (d) The discharge/charge profiles of $NiCo_2S_4$@CDs at various current densities in SIBs. (e) The comparison of rate performance between $NiCo_2S_4$@CDs electrode and different $NiCo_2S_4$-based electrode materials reported in literature. (f) Cycle performance of $NiCo_2S_4$@CDs and $NiCo_2S_4$ at 0.5 A/g in SIBs. (g) Cycle performance of $NiCo_2S_4$@CDs at 5 A/g in SIBs.

long-term cycle stability, as demonstrated in Fig. 3g, where it retains a capacity of 302.7 mAh/g after 750 cycles at 5 A/g.

To deeply study the electrochemical mechanism of the $NiCo_2S_4$@CDs electrode in SIBs, cyclic voltammetry (CV) measurements were performed at different scan rates, spanning from 0.1 mV/s to 1.0 mV/s. As shown in Fig. S3a (Supporting information), the CV curves at different scan rates are essentially identical except for the position shift of the oxidation–reduction peak, indicating the existence of pseudocapacitance behavior of $NiCo_2S_4$@CDs electrode during cycling. To confirm this behavior, a linear fitting of log(scan rate) and log(peak current) values was conducted. The slope obtained from the fitting reflects the state of the electrochemical reaction process. Typically, a slope value of 0.5 indicates that the charge–discharge process is governed by ion diffusion, while a value of 1.0 suggests that the charge–discharge process is controlled by surface capacitance. As shown in Fig. S3b (Supporting information), the slopes b of the $\log(i_p)$-$\log(v)$ curves at different peak currents are 0.78 (peak 1), 0.74 (peak 2) and 0.82 (peak 3), indicating that the charge-discharge process of $NiCo_2S_4$@CDs electrode exhibits both pseudocapacitance and ion diffusion reactions. The capacitive contribution ratio of $NiCo_2S_4$@CDs electrode was tested at a scan rate of 1.0 mV/s, indicate a pseudocapacitance contribution ratio of 91.7% (Fig. S3c in Supporting information), which is consistent with expectations. Furthermore, Fig. S3d (Supporting information) displays the calculated pseudocapacitance contribution ratios at different scan rates. Upon increasing the scan rate from 0.1 mV/s to 1.0 mV/s, the proportion of pseudocapacitance contribution gradually rises from 77% to 92%. This observation suggests that the sodium storage process of the $NiCo_2S_4$@CDs electrode is primarily governed by pseudocapacitance, and this dynamic mechanism promotes the rapid sodiation/desodiation of Na^+ in the $NiCo_2S_4$@CDs electrode.

The galvanostatic intermittent titration technique (GITT) is a method based on the potentiostatic measurement to determine the chemical diffusion coefficient of electrons/ions in mixed conductors, revealing the relationship between ion diffusion rate and depth of discharge. Therefore, this technique can help us understand the complex electrode kinetics mechanism. Fig. S3e (Supporting information) shows a complete GITT curve of $NiCo_2S_4$@CDs during a single charge–discharge cycle, demonstrating the relationship between voltage and time. Based on the formula: $D = \frac{4}{\pi\tau}\left(\frac{m_B V_M}{M_B S}\right)^2\left(\frac{\Delta E_s}{\Delta E_\tau}\right)^2$, the diffusion coefficient of Na^+ can be calculated from the GITT curve. In the equation, D represents the ion diffusion coefficient, τ is the current pulse duration, and the effective mass, molar mass, molar volume, and active surface area of the electrode material are respectively denoted by m_B, M_B, V_M, and S. Additionally, the voltage changes during constant current charge/discharge are represented by ΔE_τ, while the voltage changes caused by the pulse are represented by ΔE_s. The values of τ, ΔE_t, and ΔE_s are obtained from the potential response curve of $NiCo_2S_4$@CDs during a relaxation process (Fig. S3f in Supporting information). Upon the application of a current pulse, the discharge potential of the electrode exhibits a sudden drop. Immediately following is a relaxation process, during which the potential slowly decreases (ΔE_τ) to maintain equilibrium. After a duration of τ, the current is terminated, resulting in an instantaneous increase in potential. As the electrode gradually returns to its equilibrium state, the potential once again reaches a steady value (ΔE_s). Figs. S3g and h (Supporting information) reveal that the $NiCo_2S_4$@CDs nanocomposite exhibits an ion diffusion coefficient that surpasses that of $NiCo_2S_4$ (Fig. S3i in Supporting information), indicating superior kinetic performance. Furthermore, an evident voltage drop is observed at approximately 0.5 V and 0.9 V during discharge, which can be ascribed to the conversion reaction occurring between Na^+ and $NiCo_2S_4$@CDs. This observation is consistent with the potential at which the phase transition occurs in the cyclic voltammetry (CV) curve, reinforcing the validity of this interpretation.

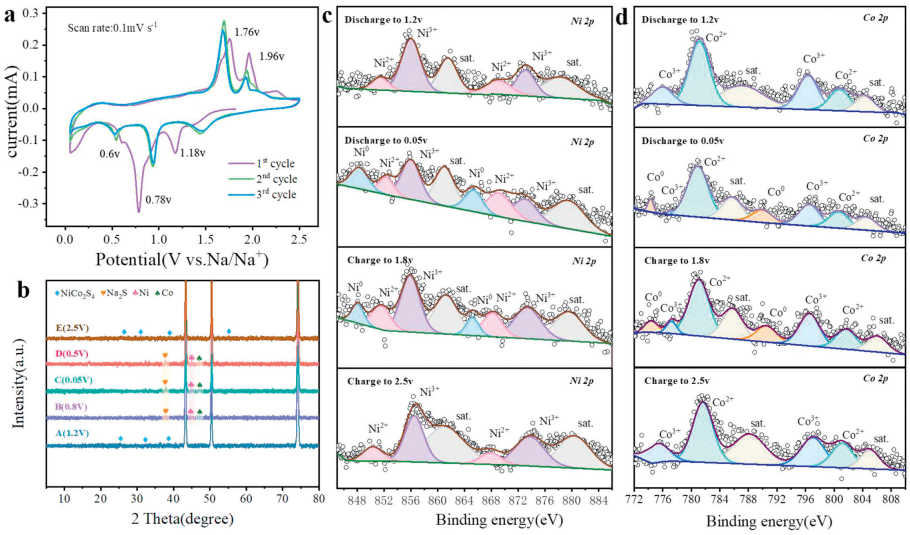

Fig. 4. (a) CV curves of $NiCo_2S_4$@CDs in SIBs. (b) *Ex-situ* XRD patterns at discharge to 1.2, 0.8, 0.05 V and charge to 0.5, 2.5 V of the $NiCo_2S_4$@CDs electrode. *Ex-situ* XPS spectra of (c) Co 2p, (d) Ni 2p at discharge to 1.2, 0.05 V and charge to 1.8, 2.5 V of the $NiCo_2S_4$@CDs electrode.

To further elucidate the factors contributing to their excellent electrochemical performance, we conducted electrochemical impedance spectroscopy (EIS) tests on the $NiCo_2S_4$@CDs and $NiCo_2S_4$ electrodes. Fig. S4a (Supporting information) shows the Nyquist plots of the $NiCo_2S_4$@CDs electrode in the initial state, as well as after the 100th and 200th cycles. The charge transfer resistance (R_{ct}) was estimated by the diameter of the semicircle on the real axis, where a smaller R_{ct} corresponds to less resistance to charge transfer at the electrode-electrolyte interface. Compared to the initial state, R_{ct} gradually decreases with an increasing cycle number, indicating that R_{ct} decreases rapidly with the continuous activation of the electrode material. The low-frequency oblique line in the Nyquist plot corresponds to the Warburg impedance (Z_w) of the electrode, which represents the diffusion of Na^+ in the electrode and electrolyte. The greater the slope of the oblique line, the faster the ion diffusion. Notably, from the initial state to 100 cycles and then to 200 cycles, the slope of the oblique line in the low frequency region increases, indicating that the ion diffusion dynamics are constantly being enhanced. With continuous activation during cycling, the ion diffusion and charge transfer in the $NiCo_2S_4$@CDs electrode demonstrate a dynamic enhancement. Furthermore, the Nyquist plots of the $NiCo_2S_4$ electrode and $NiCo_2S_4$@CDs are compared in Fig. S4b (Supporting information). It is evident that the R_{ct} of the $NiCo_2S_4$@CDs electrode is smaller, and the slope of the low-frequency linear region is larger. These observations suggest that the $NiCo_2S_4$@CDs electrode exhibits superior electronic transport and ion diffusion capabilities compared to the $NiCo_2S_4$ electrode.

When compared to the $NiCo_2S_4$ electrode, the $NiCo_2S_4$@CDs electrode with carbon dots exhibits superior electrochemical performance. It is necessary to analyze the reaction mechanism of the $NiCo_2S_4$@CDs electrode material during charge and discharge processes. Firstly, the electrochemical reaction process of the $NiCo_2S_4$ and $NiCo_2S_4$@CDs composite electrode was investigated using cyclic voltammetry. The CV curves of $NiCo_2S_4$ (Fig. S5 in Supporting information) and $NiCo_2S_4$@CDs (Fig. 4a) exhibit similar peak shapes and peak potentials, indicating that they have the same redox process. The reduction peak at 1.18 V can be attributed to the intercalation of Na^+ into $NiCo_2S_4$@CDs, forming $Na_xNiCo_2S_4$@CDs. The corresponding reaction is given by $xNa^+ + NiCo_2S_4@CDs + xe^- \rightarrow Na_xNiCo_2S_4@CD$.The reduction peaks at 0.78 V to 0.6 V are due to the conversion reaction, which generates Ni, Co, and Na_2S. The corresponding reaction is $Na_xNiCo_2S_4 + (8-x)Na^+ + (8-x)e^- \rightarrow Ni + 2Co + 4Na_2S$ [23,24,44]. Two oxidation peaks are observed at 1.76 V and 1.96 V during the anodic scan, indicating the reverse reaction of the conversion process and the deintercalation of Na^+. In the second and third cathodic scans, the cathodic peak potentials shift noticeably compared to the first cycle due to the irreversible phase transformation and structural evolution of $NiCo_2S_4$@CDs. However, the CV curves of the $NiCo_2S_4$@CDs electrode almost completely overlap after the first cycle, indicating its excellent electrochemical reversibility.

Subsequently, *ex-situ* XRD and *ex-situ* XPS measurements were implemented to examine the phase change of $NiCo_2S_4$@CDs electrode during oxidation and reduction. X-ray diffraction analysis was performed on the $NiCo_2S_4$@CDs electrode material at different voltage states under 0.2 A/g, and the *ex-situ* XRD characterization observations are presented in Fig. 4b. During discharge to 1.2 V, the $NiCo_2S_4$@CDs phase still exists due to the intercalation of Na^+. However, upon further discharge to 0.8 V to 0.05 V, the $NiCo_2S_4$@CDs phase disappears, and new Co, Ni, and Na_2S phases emerge upon reaction with Na^+. The diffraction peak located at 44.9° can be attributed to the (011) plane of metallic Ni (JCPDS card No. 45-1027), whereas the peak observed at 47.3° corresponds to the (101) plane of metallic Co (JCPDS card No. 05-0727). In addition, the characteristic peak at 37.89° belongs to the (542) plane of Na_2S (JCPDS card No. 47-1078). When charged to 0.5 V, the Co, Ni, and Na_2S phases still exist. With the proceeding of the reverse reaction and Na^+ extraction until full charging, the Co, Ni, and Na_2S phases are completely eliminated, while new diffraction peaks appearing at 38.56°, 31.0°, 26.4°, and 55.23° correspond to the (400), (311), (220), and (440) planes of $NiCo_2S_4$@CDs, confirming the reversibility of $NiCo_2S_4$@CDs and corresponding to the oxidation–reduction process reflected in the CV curve.

The reaction mechanism of $NiCo_2S_4$@CDs was further verified by *ex-situ* XPS (Figs. 4c and d). Compared to the original Ni 2p spectrum in Fig. 2b, the Ni^{2+} and Ni^{3+} bands remain consistent when discharged to 1.2 V. At 0.05 V discharge, the Ni^{2+} and Ni^{3+} bands decrease, and a new Ni^0 band appears at 848.2 and 865.2 eV [8,43]. When charged to 1.8 V, the Ni^0 band still exists due to the incomplete reverse reaction. At 2.5 V full charge, the Ni^0 band disappears, and the Ni^{2+} and Ni^{3+} bands reappear. In the Co 2p spectrum, compared to the original state in Fig. 2c, Co^{3+} gradually decreases during discharge, confirming the occurrence of reduction. A new metallic Co^0 (774.3/789.8 eV) is observed during the reaction [8,45]. The charge proceeds until full charge, and Co^{2+} and Co^{3+} are restored to the initial state, indicating reversibility. The *ex-situ*

XPS findings are consistent with the *ex-situ* XRD results, providing further support for the intercalation/conversion reaction mechanism of $NiCo_2S_4$@CDs.

In summary, cobalt–nickel bimetal coordination polymer with nanosheets cross-stacked architecture has been successfully prepared as precursor *via* simple co-precipitation reaction. Subsequently, high-temperature sulfidation method and carbon dots loading processes were successively adopted to prepare the final $NiCo_2S_4$@CDs. Due to the synergistic effects of Co/Ni based bimetallic sulfides, the introduction of carbon dots and the unique cross-stacked architecture, $NiCo_2S_4$@CDs demonstrates a higher discharge specific capacity compared to pure $NiCo_2S_4$. Furthermore, $NiCo_2S_4$@CDs also delivers an ultra-long cycle life with a discharge specific capacity of 302.9 mAh/g after 750 cycles at 5.0 A/g. Besides, *ex-situ* XRD and *ex-situ* XPS were further applied to investigate the sodium storage process of $NiCo_2S_4$@CDs. The obtained results were in line with the above-mentioned electrochemical and battery property results. This study presents an effective approach for the development of high-performance anode materials for SIBs.

Declaration of competing interest

The authors declare that they have no known competing financial interests or personal relationships that could have appeared to influence the work reported in this paper.

Acknowledgments

This work was supported by National Natural Science Foundation of China (No. 52101243), Natural Science Foundation of Guangdong Province (No. 2023A1515012619) and the Science and Technology Planning Project of Guangzhou (No. 202201010565).

Supplementary materials

Supplementary material associated with this article can be found, in the online version, at doi:10.1016/j.cclet.2023.108921.

References

[1] M. Guo, S.Y. Dong, J. Xiong, et al., Mater. Today Chem. 30 (2023) 101552.
[2] P.F. Wan, S.Y. Dong, J. Xiong, et al., J. Colloid Interface Sci. 650 (2023) 582–592.
[3] M. Guo, J. Xiong, X.Y. Jin, et al., J. Membr. Sci. 675 (2023) 121533.
[4] M. Guo, H.Y. Zhu, P.F. Wan, et al., Adv. Fiber Mater. 6 (2022) 1511–1524.
[5] P. Wei, X. Sun, Z. He, et al., Fuel 339 (2023) 127303.
[6] M.Q. Wang, B.Y. Qin, S.M. Wu, et al., J. Colloid Interface Sci. 650 (2023) 1457–1465.
[7] S.M. Wu, F. Xu, Y.N. Li, et al., J. Colloid Interface Sci. 649 (2023) 741–749.
[8] H. Zhao, J. Zhong, Y. Qi, et al., Chem. Eng. J. 465 (2023) 143032.
[9] H.S. Zhao, Y.L. Qi, K. Liang, et al., Rare Met. 41 (2021) 1284–1293.
[10] K. Liang, H. Zhao, J. Li, et al., Small 19 (2023) 2207562.
[11] M.Q. Wang, B.Y. Qin, F. Xu, et al., J. Colloid Interface Sci. 650 (2023) 446–455.
[12] B.Y. Qin, M.Q. Wang, Z.T. Liu, et al., J. Colloid Interface Sci. 646 (2023) 597–605.
[13] Y. Miao, X. Zhao, X. Wang, et al., Nano Res. 13 (2020) 3041–3047.
[14] X.Y. Yu, X.W. David Lou, Adv. Energy Mater. 8 (2018) 1701592.
[15] F. Wang, X. Liu, G. Duan, et al., Small 17 (2021) 2102532.
[16] M. Yousaf, U. Naseer, I. Ali, et al., Sci. China Mater. 65 (2021) 559–592.
[17] J. Li, J. Zhou, Q. Zhou, et al., J. Mater. Sci. Technol. 82 (2021) 114–121.
[18] B. Liu, D. Kong, Y. Wang, et al., FlatChem 10 (2018) 14–21.
[19] Y. Zhu, J. Li, X. Yun, et al., Nano-Micro Lett. 12 (2020) 16.
[20] S. Li, P. Ge, F. Jiang, et al., Energy Storage Mater. 16 (2019) 267–280.
[21] J. Yu, D. Cai, J. Si, et al., J. Mater. Chem. A 10 (2022) 4100–4109.
[22] X. Zhou, Y. Wang, C. Gong, et al., Chem. Eng. J. 402 (2020) 126189.
[23] Z. Sun, C. Zhao, X. Cao, et al., Electrochim. Acta 338 (2020) 135900.
[24] S. Fan, H. Liu, S. Bi, et al., Electrochim. Acta 388 (2021) 138618.
[25] J.S. Wei, H. Ding, P. Zhang, et al., Small 12 (2016) 5927–5934.
[26] H. Hou, C.E. Banks, M. Jing, et al., Adv. Mater. 27 (2015) 7861–7866.
[27] L. Zhang, Y. Yang, M.A. Ziaee, et al., ACS Appl. Mater. Interfaces 10 (2018) 9460–9467.
[28] X. Li, M. Rui, J. Song, et al., Adv. Funct. Mater. 25 (2015) 4929–4947.
[29] G. Cai, P. Yan, L. Zhang, et al., Chem. Rev. 121 (2021) 12278–12326.
[30] G. Chakraborty, I.H. Park, R. Medishetty, et al., Chem. Rev. 121 (2021) 3751–3891.
[31] H. Zhu, S. Dong, J. Xiong, et al., J. Colloid Interface Sci. 641 (2023) 942–949.
[32] J. Li, N. Xu, Q. Han, et al., J. Alloys Compd. 927 (2022) 167067.
[33] B. Guo, T. Yang, W. Du, et al., J. Mater. Chem. A 7 (2019) 12276–12282.
[34] H. Chen, X. Ma, P.K. Shen, Chem. Eng. J. 364 (2019) 167–176.
[35] R. Zhai, Y. Xiao, T. Ding, et al., J. Alloys Compd. 845 (2020) 156164.
[36] C. Zhang, X. Cai, Y. Qian, et al., Adv. Sci. 5 (2018) 170037.
[37] X. Li, H. Liang, B. Qin, et al., J. Colloid Interface Sci. 625 (2022) 41–49.
[38] B. Li, C. Song, J. Rong, et al., J. Energy Chem. 50 (2020) 195–205.
[39] J. Li, X. Yun, Z. Hu, et al., J. Mater. Chem. A 7 (2019) 26311–26325.
[40] R. Jia, F. Zhu, S. Sun, et al., J. Power Sources 341 (2017) 427–434.
[41] J.Y. Lin, S.J. Lu, Y.F. Zhang, et al., J. Colloid Interface Sci. 645 (2023) 654–662.
[42] C. Liu, X. Wu, B. Wang, Chem. Eng. J. 392 (2020) 123651.
[43] T. Li, Y. Xia, H. Wu, et al., Nanoscale 14 (2022) 10226–10235.
[44] T. Xu, J. Zhao, J. Yang, et al., Ionics (Kiel) 26 (2019) 213–221.
[45] J. Xiong, X.Y. Liu, P. Xia, et al., J. Colloid Interf. Sci. 652 (2023) 1417–1426.